



Universiteit Gent
Faculteit Wetenschappen
Vakgroep Fysica en Sterrenkunde

2 No title yet

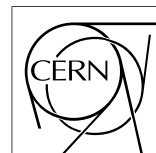
3 No sub-title neither, obviously...

4 Alexis Fagot

5



Thesis to obtain the degree of
Doctor of Philosophy in Physics
Academic years 2012-2017





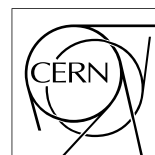
Universiteit Gent
Faculteit Wetenschappen
Vakgroep Fysica en Sterrenkunde

7
8 Promotoren: Dr. Michael Tytgat
Prof. Dr. Dirk Ryckbosch

9
10 Universiteit Gent
11 Faculteit Wetenschappen
12
13 Vakgroep Fysica en Sterrenkunde
14 Proeftuinstraat 86, B-9000 Gent, België
15 Tel.: +32 9 264.65.28
16 Fax.: +32 9 264.66.97



Thesis to obtain the degree of
Doctor of Philosophy in Physics
Academic years 2012-2017



Acknowledgements

19 Ici on remerciera tous les gens que j'ai pu croiser durant cette aventure et qui m'ont
20 permis de passer un bon moment

21 *Gent, ici la super date de la mort qui tue de la fin d'écriture*
22 *Alexis Fagot*

Table of Contents

24	Acknowledgements	i
25	Nederlandse samenvatting	xv
26	English summary	xvii
27	1 Introduction	1-1
28	1.1 A story of High Energy Physics	1-1
29	1.2 Organisation of this study	1-1
30	2 Investigating the TeV scale	2-1
31	2.1 The Standard Model of Particle Physics	2-1
32	2.2 The Large Hadron Collider and the Compact Muon Solenoid . . .	2-1
33	2.3 Muon Phase-II Upgrade	2-1
34	3 Amplification processes in gaseous detectors	3-1
35	3.1 Signal formation	3-1
36	3.2 Gas transport parameters	3-1
37	4 Resistive Plate Chambers	4-1
38	4.1 Principle	4-1
39	4.2 Rate capability of Resistive Plate Chambers	4-1
40	4.3 High time resolution	4-1
41	4.4 Resistive Plate Chambers at CMS	4-1
42	5 Investigation on high rate RPCs	5-1
43	5.1 Rate limitations and ageing of RPCs	5-1
44	5.1.1 Low resistivity electrodes	5-1
45	5.1.2 Low noise front-end electronics	5-1
46	5.2 Construction of prototypes	5-1
47	5.3 Results and discussions	5-1
48	6 Consolidation and Research and Development approval	6-1
49	6.1 Testing detectors under extreme conditions	6-1
50	6.1.1 High Luminosity LHC	6-1
51	6.1.2 The Gamma Irradiation Facilities	6-2

52	6.1.2.1	GIF	6-2
53	6.1.2.2	GIF++	6-3
54	6.2	Preliminary consolidation tests at GIF	6-4
55	6.2.1	Resistive Plate Chamber test setup	6-4
56	6.2.2	Data Acquisition	6-7
57	6.2.3	Geometrical acceptance of the setup layout to cosmic muons	6-7
58	6.2.3.1	Description of the simulation layout	6-9
59	6.2.3.2	Simulation procedure	6-11
60	6.2.3.3	Results	6-12
61	6.2.4	Photon flux at GIF	6-12
62	6.2.4.1	Expectations from simulations	6-12
63	6.2.4.2	Dose measurements	6-16
64	6.3	Longevity tests at GIF++	6-17
65	6.3.1	Description of the Data Acquisition	6-18
66	6.3.1.1	GIF++ RPC DAQ	6-22
67	6.3.1.2	RPC current, environmental and operation pa- rameter monitoring	6-23
68	6.3.2	Tools & Measurements	6-23
69	6.4	Results and discussions	6-23
70	6.4.1	Preliminary studies results	6-23
71	6.4.2	Longevity studies results	6-24
72			
73	7	Simulating a RPC	7-1
74	7.1	Garfield++ simulation	7-1
75	7.2	Hybrid simulation	7-1
76	7.3	Results and discussions	7-1
77	8	Conclusions and outlooks	8-1
78	8.1	Conclusions	8-1
79	8.2	Outlooks	8-1
80	A	A data acquisition software for VME CAEN TDCs	A-1
81	A.1	Introduction	A-1
82	B	Details on the online analysis package	B-1
83	B.1	Introduction	B-1
84	C	Structure of the hybrid simulation software	C-1
85	C.1	Introduction	C-1

List of Figures

87	2.1	Absorbed dose in the CMS cavern after an integrated luminosity	
88		of 3000 fb. R is the transverse distance from the beamline and Z is	
89		the distance along the beamline from the Interaction Point at Z=0.	2-2
90	2.2	A quadrant of the muon system, showing DTs (yellow), RPCs	
91		(light blue), and CSCs (green). The locations of new forward	
92		muon detectors for Phase-II are contained within the dashed box	
93		and indicated in red for GEM stations (ME0, GE1/1, and GE2/1)	
94		and dark blue for improved RPC (iRPC) stations (RE3/1 and RE4/1).	2-3
95	2.3	RMS of the multiple scattering displacement as a function of muon	
96		p_T for the proposed forward muon stations. All of the electromag-	
97		netic processes such as bremsstrahlung and magnetic field effect	
98		are included in the simulation.	2-3
99	6.1	The plots represent the RPC rate measured in 2016 in p - p colli-	
100		sion runs as function of the instantaneous luminosity. Every point	
101		corresponds to a particular run.	6-2
102	6.2	Layout of the test beam zone called X5c GIF at CERN. Photons	
103		from the radioactive source produce a sustained high rate of ran-	
104		dom hits over the whole area. The zone is surrounded by 8 m high	
105		and 80 cm thick concrete walls. Access is possible through three	
106		entry points. Two access doors for personnel and one large gate	
107		for material. A crane allows installation of heavy equipment in the	
108		area.	6-3
109	6.3	^{137}Cs decays by β^- emission to the ground state of ^{137}Ba (BR =	
110		5.64%) and via the 662 keV isomeric level of ^{137}Ba (BR = 94.36%)	
111		whose half-life is 2.55 min.	6-4
112	6.4	Description of the RPC setup. Dimensions are given in mm. Fig-	
113		ure 6.4a provides a side view of the setup while Figure 6.4b shows	
114		a top view. A tent containing RPCs is placed at 1720 mm from	
115		the source container. The source is situated in the center of the	
116		container. RE-4-2-BARC-161 chamber is 160 mm inside the tent.	
117		This way, the distance between the source and the chambers plan	
118		is 2060 mm.	6-5

119	6.5	RE-4-2-BARC-161 chamber is inside the tent as described in Figure 6.4. In the top right, the two scintillators used as trigger can be seen. This trigger system has an inclination of 10° relative to horizontal and is placed above half-partition B2 of the RPC. PMTs' electronics are shielded thanks to lead blocks placed in order to protect them without stopping photons from going through the scintillators and the chamber.	6-5
120			
121			
122			
123			
124			
125			
126	6.6	Hit distributions over all 3 partitions of RE-4-2-BARC-161 chamber is showed on these plots. Top, middle and bottom figures respectively correspond to partitions A, B, and C. These plots show that some events still occur in other half-partitions than B2, which corresponds to strips 49 to 64, in front of which the trigger is placed, contributing to the inefficiency of detection of cosmic muons. In the case of partitions A and C, the very low amount of data can be interpreted as noise. On the other hand, it is clear that a little portion of muons reach the half-partition B1, corresponding to strips 33 to 48.	6-6
127			
128			
129			
130			
131			
132			
133			
134			
135			
136	6.7	Signals from the RPC strips are shaped by the FEE described on Figure 6.7a. Output LVDS signals are then read-out by a TDC module connected to a computer or converted into NIM and sent to scalers. Figure 6.7b describes how these converted signals are put in coincidence with the trigger.	6-7
137			
138			
139			
140			
141	6.8	Description of the principle of a CFD. A comparison of threshold triggering (left) and constant fraction triggering (right) is shown in Figure 6.8a. Constant fraction triggering is obtained thanks to zero-crossing technique as explained in Figure 6.8b. The signal arriving at the input of the CFD is split into three components. A first one is delayed and connected to the inverting input of a first comparator. A second component is connected to the noninverting input of this first comparator. A third component is connected to the noninverting input of another comparator along with a threshold value connected to the inverting input. Finally, the output of both comparators is fed through an AND gate.	6-8
142			
143			
144			
145			
146			
147			
148			
149			
150			
151			
152	6.9	Results are derived from data taken on half-partition B2 only. On the 18 th of June 2014, data has been taken on chamber RE-2-BARC-161 at building 904 (Preessin Site) with cosmic muons providing us a reference efficiency plateau of $(97.54 \pm 0.15)\%$ represented by a black curve. A similar measurement has been done at GIF on the 21 st of July with the same chamber giving a plateau of $(78.52 \pm 0.94)\%$ represented by a red curve.	6-9
153			
154			
155			
156			
157			
158			

159	6.10 Representation of the layout used for the simulations of the test	
160	setup. The RPC is represented as a yellow trapezoid while the two	
161	scintillators as blue cuboids looking at the sky. A green plane cor-	
162	responds to the muon generation plane within the simulation. Fig-	
163	ure 6.4a shows a global view of the simulated setup. Figure 6.4b	
164	shows a zoomed view that allows to see the 2 scintillators as well	
165	as the full RPC plane.	6-10
166	6.11 γ flux $F(D)$ is plot using values from table 6.1. As expected, the	
167	plot shows similar attenuation behaviours with increasing distance	
168	for each absorption factors.	6-13
169	6.12 Figure 6.12a shows the linear approximation fit done via formu-	
170	lae 6.7 on data from table 6.2. Figure 6.12b shows a comparison	
171	of this model with the simulated flux using a and b given in fig-	
172	ure 6.12a in formulae 6.4 and the reference value $D_0 = 50cm$	
173	and the associated flux for each absorption factor F_0^{ABS} from ta-	
174	ble 6.1	6-15
175	6.13 Dose measurements has been done in a plane corresponding to the	
176	tents front side. This plan is 1900 mm away from the source. As	
177	explained in the first chapter, a lens-shaped lead filter provides a	
178	uniform photon flux in the vertical plan orthogonal to the beam	
179	direction. If the second line of measured fluxes is not taken into	
180	account because of lower values due to experimental equipments	
181	in the way between the source and the tent, the uniformity of the	
182	flux is well showed by the results.	6-17
183	6.14 Evolution of the maximum efficiency for RE2 (6.14a) and RE4	
184	(6.14b) chambers with increasing extrapolated γ rate per unit area	
185	at working point. Both irradiated (blue) and non irradiated (red)	
186	chambers are shown.	6-19
187	6.15 Evolution of the working point for RE2 (6.15a) and RE4 (6.15b)	
188	with increasing extrapolated γ rate per unit area at working point.	
189	Both irradiated (blue) and non irradiated (red) chambers are shown.	6-19
190	6.16 Evolution of the maximum efficiency at HL-LHC conditions, i.e.	
191	a background hit rate per unit area of 300 Hz/cm^2 , with increasing	
192	integrated charge for RE2 (6.16a) and RE4 (6.16b) detectors. Both	
193	irradiated (blue) and non irradiated (red) chambers are shown. The	
194	integrated charge for non irradiated detectors is recorded during	
195	test beam periods and stays small with respect to the charge accu-	
196	culated in irradiated chambers.	6-20
197	6.17 Comparison of the efficiency sigmoid before (triangles) and after	
198	(circles) irradiation for RE2 (6.17a) and RE4 (6.17b) detectors.	
199	Both irradiated (blue) and non irradiated (red) chambers are shown.	6-20
200	6.18 Evolution of the Bakelite resistivity for RE2 (6.18a) and RE4 (6.18b)	
201	detectors. Both irradiated (blue) and non irradiated (red) chambers	
202	are shown.	6-21

203	6.19 Evolution of the noise rate per unit area for the irradiated chamber	
204	RE2-2-BARC-9 only.	6-21
205	6.20	6-23

List of Tables

207	6.1	Total photon flux ($E\gamma \leq 662$ keV) with statistical error predicted	
208		considering a ^{137}Cs activity of 740 GBq at different values of the	
209		distance D to the source along the x-axis of irradiation field [4]. . .	6-13
210	6.2	Correction factor c is computed thanks to formulae 6.5 taking as	
211		reference $D_0 = 50$ cm and the associated flux F_0^{ABS} for each ab-	
212		sorption factor available in table 6.1.	6-14
213	6.3	The data at D_0 in 1997 is taken from [4]. In a second step, using	
214		Equations 6.8 and 6.9, the flux at D can be estimated in 1997.	
215		Then, taking into account the attenuation of the source activity,	
216		the flux at D can be estimated at the time of the tests in GIF in	
217		2014. Finally, assuming a sensitivity of the RPC to γ $s = 2 \cdot 10^{-3}$,	
218		an estimation of the hit rate per unit area is obtained.	6-16

List of Acronyms

List of Acronyms

B

225 BARC

Bhabha Atomic Research Centre

226 BR

Branching Ratio

C

231 CAEN

Costruzioni Apparecchiature Elettroniche Nucleari S.p.A.

233 CERN

European Organization for Nuclear Research

234 CFD

Constant Fraction Discriminator

235 CMS

Compact Muon Solenoid

236 CSC

Cathode Strip Chamber

D

241 DAQ

Data Acquisition

242 DCS

Detector Control Software

243 DQM

Data Quality Monitoring

244 DT

Drift Tube

F

249 FEE

Front-End Electronics

250	FEB	Front-End Board
251		
252		
253	G	
254		
255	GE-/-	Find a good description
256	GE1/1	Find a good description
257	GE2/1	Find a good description
258	GEANT	GEometry ANd Tracking - <i>a series of software toolkit platforms developed by CERN</i>
259		
260	GEM	Gas Electron Multiplier
261	GIF	old Gamma Irradiation Facility dismantled in 2014
262	GIF++	new Gamma Irradiation Facility
263		
264		
265	H	
266		
267	HL-LHC	High Luminosity LHC
268	HV	High Voltage
269		
270		
271	I	
272		
273	iRPC	improved RPC
274		
275		
276	L	
277		
278	LHC	Large Hadron Collider
279	LS1	First Long Shutdown
280	LS3	Third Long Shutdown
281	LV	Low Voltage
282	LVDS	Low-Voltage Differential Signaling
283		
284		
285	M	
286		
287	MC	Monte Carlo

288	MCNP	Monte Carlo N-Particle
289	ME-/-	Find good description
290	ME0	Find good description
291		
292		
293	N	
294		
295	NIM	Nuclear Instrumentation Module logic signals
296		
297		
298	P	
299		
300	PMT	PhotoMultiplier Tube
301		
302		
303	R	
304		
305	RE-/-	Find a good description
306	RE2/2	Find a good description
307	RE3/1	Find a good description
308	RE3/2	Find a good description
309	RE4/1	Find a good description
310	RE4/2	Find a good description
311	RE4/3	Find a good description
312	RMS	Root Mean Square
313	ROOT	<i>a framework for data processing born at CERN</i>
314	RPC	Resistive Plate Chamber
315		
316		
317	S	
318		
319	SPS	Super Proton Synchrotron
320		
321		
322	T	
323		
324	TDC	Time-to-Digital Converter

326

Nederlandse samenvatting –Summary in Dutch–

327

328 Le resume en Neerlandais (j'aurais peut-etre de apprendre la langue juste pour
329 ca...).

English summary

331 Le meme résumé mais en Anglais (on commencera par la hein!).

1

Introduction

332

333

334 **1.1 A story of High Energy Physics**

335 **1.2 Organisation of this study**

2

Investigating the TeV scale

2.1 The Standard Model of Particle Physics

2.2 The Large Hadron Collider and the Compact Muon Solenoid

2.3 Muon Phase-II Upgrade

After the more than two years lasting First Long Shutdown (LS1), the Large Hadron Collider (LHC) delivered its very first Run-II proton-proton collisions early 2015. LS1 gave the opportunity to the LHC and to the its experiments to undergo upgrades. The accelerator is now providing collisions at center-of-mass energy of 13 TeV and bunch crossing rate of 40 MHz, with a peak luminosity exceeding its design value. During the first and upcoming second LHC Long Shutdown, the Compact Muon Solenoid (CMS) detector is also undergoing a number of upgrades to maintain a high system performance [1].

From the LHC Phase-2 or High Luminosity LHC (HL-LHC) period onwards, i.e. past the Third Long Shutdown (LS3), the performance degradation due to integrated radiation as well as the average number of inelastic collisions per bunch crossing, or pileup, will rise substantially and become a major challenge for the LHC experiments, like CMS that are forced to address an upgrade program for Phase-II [2]. Simulations of the expected distribution of absorbed dose in the CMS detector under HL-LHC conditions, show in figure 6.13 that detectors placed close

to the beamline will have to withstand high irradiation, the radiation dose being of the order of a few tens of Gy.

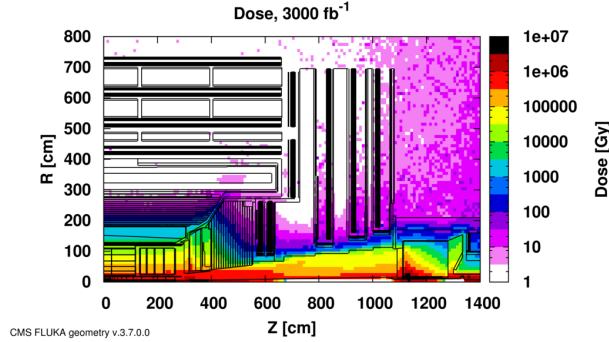


Figure 2.1: Absorbed dose in the CMS cavern after an integrated luminosity of 3000 fb. R is the transverse distance from the beamline and Z is the distance along the beamline from the Interaction Point at $Z=0$.

The measurement of small production cross-section and/or decay branching ratio processes, such as the Higgs boson coupling to charge leptons or the $B_s \rightarrow \mu^+ \mu^-$ decay, is of major interest and specific upgrades in the forward regions of the detector will be required to maximize the physics acceptance on the largest possible solid angle. To ensure proper trigger performance within the present coverage, the muon system will be completed with new chambers. In figure 2.2 one can see that the existing Cathode Strip Chamber (CSC) modules will be completed by Gas Electron Multipliers (GEMs) and Resistive Plate Chambers (RPCs) in the pseudo-rapidity region $1.6 < |\eta| < 2.4$ to complete its redundancy as originally scheduled in the CMS Technical Proposal [3].

RPCs are used by the CMS first level trigger for their good timing performances. Indeed, a very good bunch crossing identification can be obtained with the present CMS RPC system, given their fast response of the order of 1 ns. In order to contribute to the precision of muon momentum measurements, muon chambers should have a spatial resolution less or comparable to the contribution of multiple scattering [1]. Most of the plausible physics is covered only considering muons with $p_T < 100$ GeV thus, in order to match CMS requirements, a spatial resolution of $\mathcal{O}(\text{few mm})$ the proposed new RPC stations, as shown by the simulation in figure 2.3. According to preliminary designs, RE3/1 and RE4/1 readout pitch will be comprised between 3 and 6 mm and 5 η -partitions could be considered.

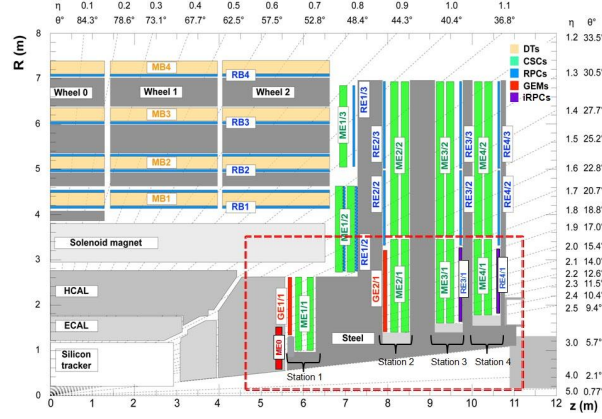


Figure 2.2: A quadrant of the muon system, showing DTs (yellow), RPCs (light blue), and CSCs (green). The locations of new forward muon detectors for Phase-II are contained within the dashed box and indicated in red for GEM stations (ME0, GE1/1, and GE2/1) and dark blue for improved RPC (iRPC) stations (RE3/1 and RE4/1).

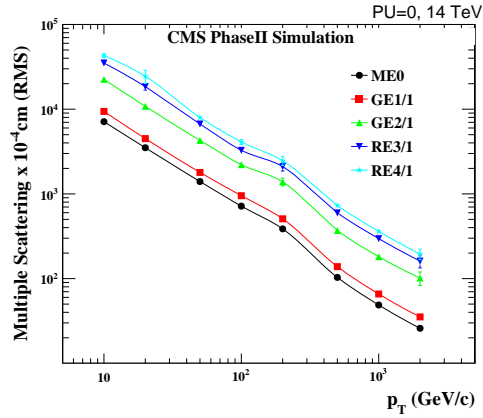


Figure 2.3: RMS of the multiple scattering displacement as a function of muon p_T for the proposed forward muon stations. All of the electromagnetic processes such as bremsstrahlung and magnetic field effect are included in the simulation.

3

379

380

Amplification processes in gaseous detectors

381

382

3.1 Signal formation

383

3.2 Gas transport parameters

4

384

385

Resistive Plate Chambers

386 **4.1 Principle**

387 **4.2 Rate capability of Resistive Plate Chambers**

388 **4.3 High time resolution**

389 **4.4 Resistive Plate Chambers at CMS**

5

390

391

Investigation on high rate RPCs

392 **5.1 Rate limitations and ageing of RPCs**

393 **5.1.1 Low resistivity electrodes**

394 **5.1.2 Low noise front-end electronics**

395 **5.2 Construction of prototypes**

396 **5.3 Results and discussions**

6

Consolidation and Research and Development approval

6.1 Testing detectors under extreme conditions

6.1.1 High Luminosity LHC

The upgrade from LHC to HL-LHC will increase the peak luminosity from $10^{34} \text{ cm}^{-2} \text{ s}^{-1}$ to reach $7.5 \times 10^{34} \text{ cm}^{-2} \text{ s}^{-1}$, increasing in the same way the total expected background to which the RPC system will be subjected to. Composed of low energy gammas and neutrons from p - p collisions, low momentum primary and secondary muons, punch-through hadrons from calorimeters, and particles produced in the interaction of the beams with collimators, the background will mostly affect the regions of CMS that are the closest to the beam line, i.e. the RPC detectors located in the endcaps.

The information collected with 2016 data allowed us to understand that the hottest RPC regions are located in the fourth endcap stations. Extrapolating from the data shown in Figure 6.1, the maximum rate per unit area under HL-LHC conditions is therefore foreseen to increase to values of the order of 400 Hz/cm^2 in the chambers of the present muon system. To the 4000 fb^{-1} of integrated luminosity, over the 10 years of HL-LHC lifetime, will correspond $\sim 0.4 \text{ C/cm}^2$ of integrated charge inside the hottest regions of the detectors.

During Run-I, the RPC system provided stable operation and excellent performance and did not show any aging effects. In the past, extensive long-term tests

were carried out at several gamma and neutron facilities certifying the detector performance up to values of dose, charge and fluence close to those expected after ten years of HL-LHC operation. Both full size and small prototype RPCs have been irradiated with photons up to an integrated charge of $\sim 0.05 \text{ C/cm}^2$ and $\sim 0.4 \text{ C/cm}^2$, respectively [5, 6].

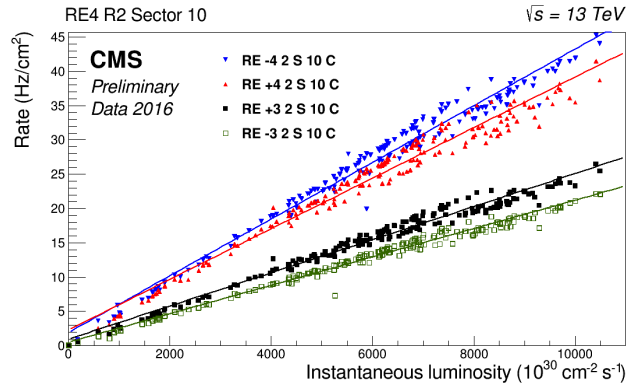


Figure 6.1: The plots represent the RPC rate measured in 2016 in p - p collision runs as function of the instantaneous luminosity. Every point corresponds to a particular run.

In this perspective, studying the performance of the present system up to an integrated charge of $\sim 1.2 \text{ C/cm}^2$, 3 times higher than what expected for 10 years of operation of HL-LHC, and background hit rates of 1200 Hz/cm^2 , 3 times stronger than what expected from the designed peak luminosity, and identifying possible long-term aging effects are necessary steps to take to insure that the RPCs will be able to cope with the high radiation conditions.

6.1.2 The Gamma Irradiation Facilities

6.1.2.1 GIF

GIF was a test area located in the SPS West Area at the downstream end of the X5 test beam in which particle detectors were exposed to a particle beam in presence of an adjustable background flux of photons [GIFacility]. This facility's goal was to simulate background conditions these detectors would suffer in their operating environment at the LHC. A schematic layout of the GIF zone is shown in Figure 6.2. Photons are produced by a strong radioactive source of ^{137}Cs installed in the upstream part of the zone inside a lead container, which includes a collimator, designed to irradiate a $6 \times 6 \text{ m}^2$ area at 5 m distance from the source. A thin

lens-shaped lead filter renders the outcoming flux uniform in the vertical plane orthogonal to the beam direction. Control of the photon rate is achieved by further lead filters allowing the maximum rate to be limited and to vary within a range of four orders of magnitude. The Gamma source is located in a rectangular lead container.

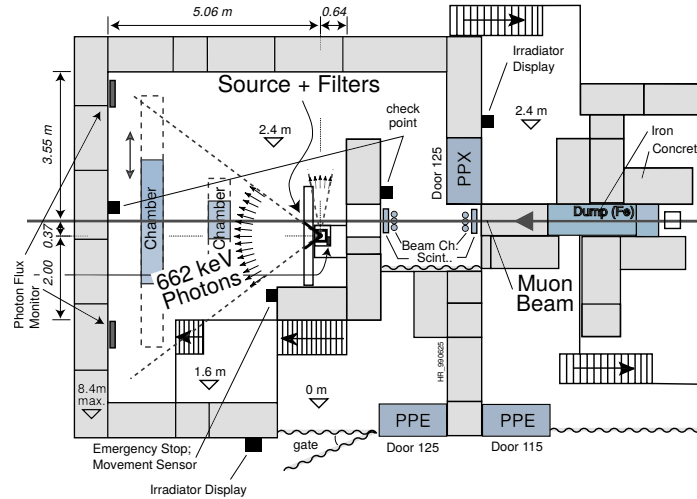


Figure 6.2: Layout of the test beam zone called X5c GIF at CERN. Photons from the radioactive source produce a sustained high rate of random hits over the whole area. The zone is surrounded by 8 m high and 80 cm thick concrete walls. Access is possible through three entry points. Two access doors for personnel and one large gate for material. A crane allows installation of heavy equipment in the area.

As described on Figure 6.3, the ^{137}Cs source with a half-life of 30 years and an activity of 740 GBq, as measured on the 5th March 1997, emits a 662 keV photon in 85% of the decays. The principal collimator hole provides a pyramidal aperture of $74^\circ \times 74^\circ$ solid angle. This provides a photon flux in a pyramidal volume of 5 m maximum length along the beam axis.

Particle detectors under test are then placed within the pyramidal volume in front of the source, perpendicularly to the beam line in order to profit from the homogeneous photon flux. Adjusting the background flux of photons can then be done by using the filters and choosing the position of the detectors with respect to the source.

6.1.2.2 GIF++

GIF++ is a test area located in the SPS North Area at the downstream end of the H4 test beam. In this facility, particle detectors are tested using a particle beam

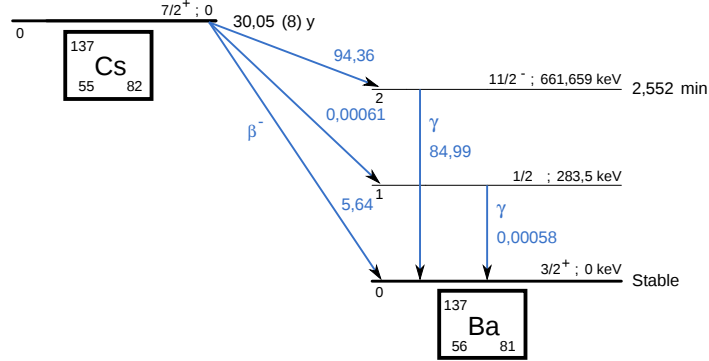


Figure 6.3: ^{137}Cs decays by β^- emission to the ground state of ^{137}Ba ($\text{BR} = 5.64\%$) and via the 662 keV isomeric level of ^{137}Ba ($\text{BR} = 94.36\%$) whose half-life is 2.55 min.

in presence of an adjustable background flux of photons. The goal is to simulate background conditions these detectors would suffer in their operating environment at the HL-LHC (**here we should show the GIF++ layout**). Gamma photons are produced by a strong radioactive ^{137}Cs source installed in the center part of the zone, with an activity of 13.1 TBq, emitting 662 keV photons. A thin lens-shaped lead filter renders the outcoming flux uniform in the vertical plane orthogonal to the beam direction. Control of the photon rate is achieved by using a set of filters allowing the maximum rate to be limited and to vary within a range of four orders of magnitude. The H4 beam, composed of muons with a momentum of about 150 GeV/c, passes through the GIF++ zone and is used to study the performance of the detectors. Its flux is of 104 particles/s/cm² focused in an area similar to $10 \times 10 \text{ cm}^2$.

6.2 Preliminary consolidation tests at GIF

6.2.1 Resistive Plate Chamber test setup

During summer 2014, preliminary tests have been conducted in the GIF area on a newly produced RE4/2 chamber labelled RE-4-2-BARC-161. This chamber has been placed into a trolley covered with a tent. The position of the RPC inside the tent and of the tent related to the source is described in Figure 6.4. To test this CMS RPC, three different absorber settings were used. First of all, measurements were done with fully opened source. Then, to complete this preliminary study, the gamma flux has been attenuated by a factor 2 and a factor 5. The expected gamma flux at the level of our detector will be discussed in subsection 6.2.4.

At the time of the tests, the beam not being operationnal anymore, a trigger

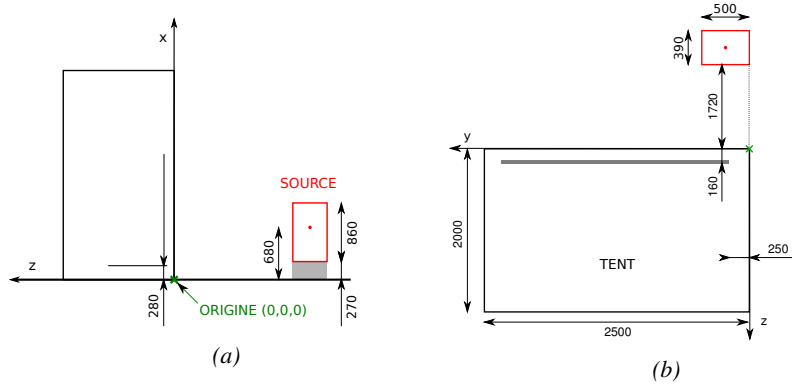


Figure 6.4: Description of the RPC setup. Dimensions are given in mm. Figure 6.4a provides a side view of the setup while Figure 6.4b shows a top view. A tent containing RPCs is placed at 1720 mm from the source container. The source is situated in the center of the container. RE-4-2-BARC-161 chamber is 160 mm inside the tent. This way, the distance between the source and the chambers plan is 2060 mm.

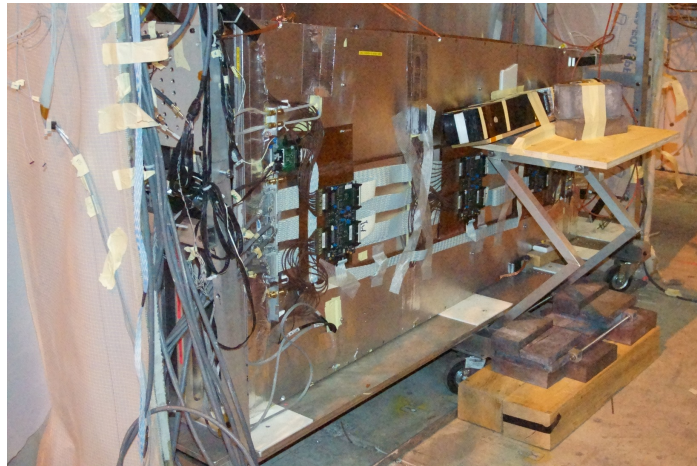


Figure 6.5: RE-4-2-BARC-161 chamber is inside the tent as described in Figure 6.4. In the top right, the two scintillators used as trigger can be seen. This trigger system has an inclination of 10° relative to horizontal and is placed above half-partition B2 of the RPC. PMTs' electronics are shielded thanks to lead blocks placed in order to protect them without stopping photons from going through the scintillators and the chamber.

483 composed of 2 plastic scintillators has been placed in front of the setup with an
 484 inclination of 10° deg (**this has to be first confirmed by the simulation - I will ad-**
 485 **just in consequence cause it has never been precisely measured**) with respect to

the detector plane in order to look at cosmic muons. Using this particular trigger layout, shown on Figure 6.5, leads to a cosmic muon hit distribution into the chamber similar to the one in Figure 6.6. Measured without gamma irradiation, two peaks can be seen on the profil of partition B, centered on strips 52 and 59. Sub-section 6.2.3 will help us understand that these two peaks are due respectively to forward and backward coming cosmic particles where forward coming particles are first detected by the scintillators and then the RPC while the backward coming muons are first detected in the RPC.

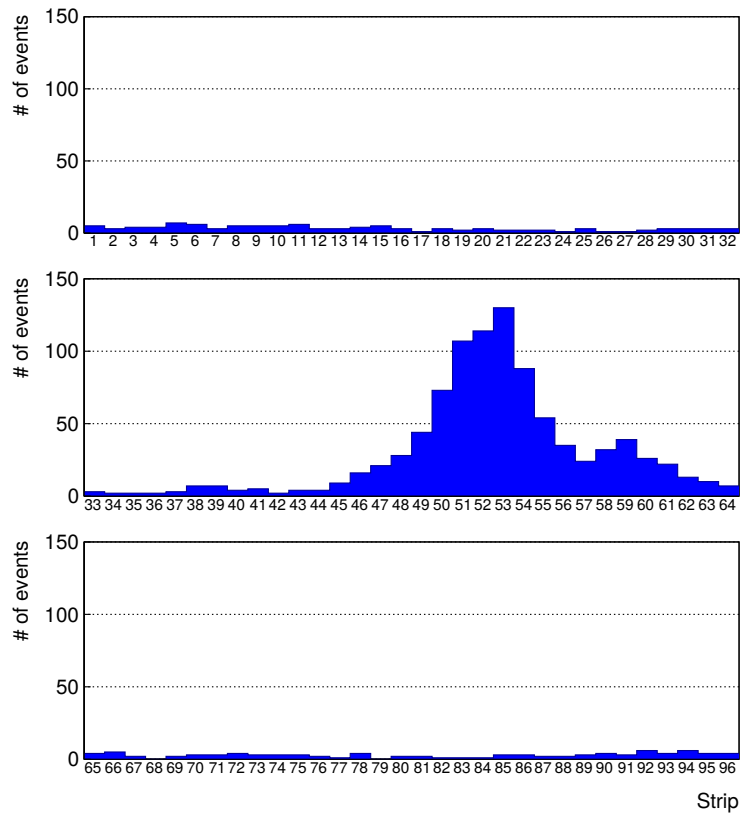


Figure 6.6: Hit distributions over all 3 partitions of RE-4-2-BARC-161 chamber is showed on these plots. Top, middle and bottom figures respectively correspond to partitions A, B, and C. These plots show that some events still occur in other half-partitions than B2, which corresponds to strips 49 to 64, in front of which the trigger is placed, contributing to the inefficiency of detection of cosmic muons. In the case of partitions A and C, the very low amount of data can be interpreted as noise. On the other hand, it is clear that a little portion of muons reach the half-partition B1, corresponding to strips 33 to 48.

6.2.2 Data Acquisition

Signals induced by cosmic particle in the RPC strips are shaped by standard CMS RPC Front-End Electronics (FEE) following the scheme of Figure 6.7. On a first stage, analogic signals are amplified and then sent to the Constant Fraction Discriminator (CFD) described in Figure 6.8. At the end of the chain, 100 ns long pulses are sent in the LVDS output. These output signal are sent on one side to a V1190A Time-to-Digital Converter (TDC) module from CAEN and on the other to an OR module to count the number of detected signals. Trigger and hit coincidences are monitored using scalars. The TDC is used to store the data into ROOT files. These ROOT files are thus analysed to understand the detectors performance.

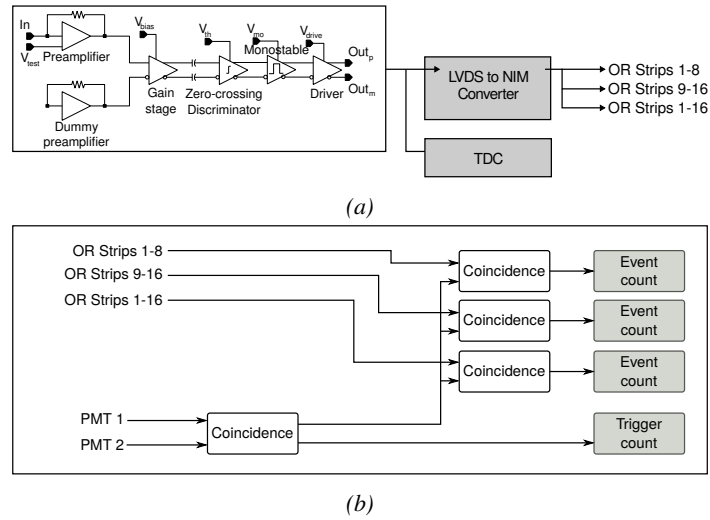


Figure 6.7: Signals from the RPC strips are shaped by the FEE described on Figure 6.7a. Output LVDS signals are then read-out by a TDC module connected to a computer or converted into NIM and sent to scalars. Figure 6.7b describes how these converted signals are put in coincidence with the trigger.

6.2.3 Geometrical acceptance of the setup layout to cosmic muons

In order to profit from a constant gamma irradiation, the detectors inside of the GIF bunker need to be placed in a plane orthogonal to the beam line. The muon beam that used to be available was meant to test the performance of detectors under test. This beam not being active anymore, another solution to test detector performance had to be used. Thus, it has been decided to use cosmic muons detected through a telescope composed of two scintillators. Lead blocks were used as shielding to protect the photomultipliers from gammas as can be seen from Figure 6.5.

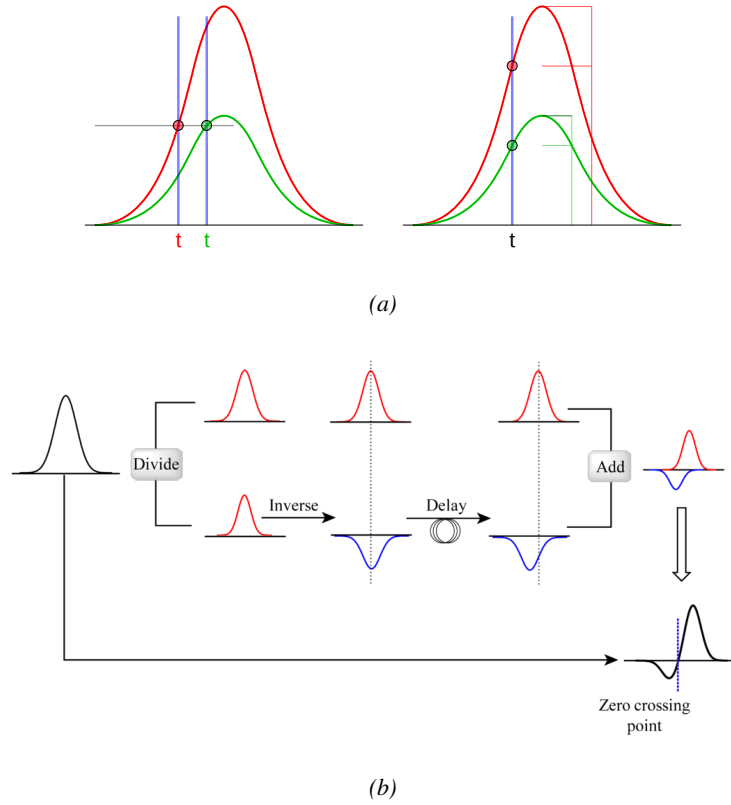


Figure 6.8: Description of the principle of a CFD. A comparison of threshold triggering (left) and constant fraction triggering (right) is shown in Figure 6.8a. Constant fraction triggering is obtained thanks to zero-crossing technique as explained in Figure 6.8b. The signal arriving at the input of the CFD is split into three components. A first one is delayed and connected to the inverting input of a first comparator. A second component is connected to the noninverting input of this first comparator. A third component is connected to the noninverting input of another comparator along with a threshold value connected to the inverting input. Finally, the output of both comparators is fed through an AND gate.

512 An inclination has been given to the cosmic telescope to maximize the muon
 513 flux. A good compromise had to be found between good enough muon flux and
 514 narrow enough hit distribution to be sure to contain all the events into only one half
 515 partitions as required from the limited available readout hardware. Nevertheless,
 516 a consequence of the misplaced trigger, that can be seen as a loss of events in
 517 half-partition B1 in Figure 6.6, is an inefficiency. Nevertheless, the inefficiency
 518 of approximately 20 % highlighted in Figure 6.9 by comparing the performance of

519 chamber BARC-161 in 904 and at GIF without irradiation seems too important to
 520 be explained only by the geometrical acceptance of the setup itself. Simulations
 521 have been conducted to show how the setup brings inefficiency.

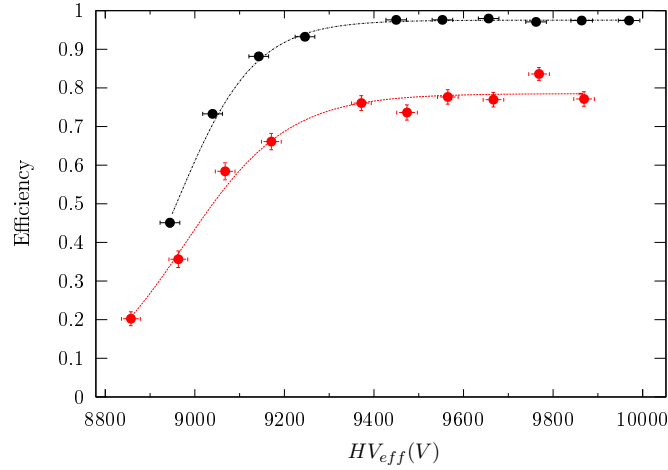


Figure 6.9: Results are derived from data taken on half-partition B2 only. On the 18th of June 2014, data has been taken on chamber RE-2-BARC-161 at building 904 (Preveessin Site) with cosmic muons providing us a reference efficiency plateau of $(97.54 \pm 0.15)\%$ represented by a black curve. A similar measurement has been done at GIF on the 21st of July with the same chamber giving a plateau of $(78.52 \pm 0.94)\%$ represented by a red curve.

522 6.2.3.1 Description of the simulation layout

523 The layout of GIF setup has been reproduced and incorporated into a Monte Carlo
 524 (MC) simulation to study the influence of the disposition of the telescope on the
 525 final distribution measured by the RPC. A 3D view of the simulated layout is given
 526 into Figure 6.10. Muons are generated randomly in a horizontal plane located at a
 527 height corresponding to the lowest point of the PMTs. This way, the needed size
 528 of the plane in order to simulate events happening at very big azimuthal angles (i.e.
 529 $\theta \approx \pi$) can be kept relatively small. The muon flux is designed to follow the usual
 530 $\cos^2\theta$ distribution for cosmic particle. The goal of the simulation is to look at
 531 muons that pass through the muon telescope composed of the two scintillators and
 532 define their distribution onto the RPC plane. During the reconstruction, the RPC
 533 plane is then divided into its strips and each muon track is assigned to a strip.

534 In order to further refine the quality of the simulation and understand deeper
 535 the results the dependance of the distribution has been studied for a range of tele-

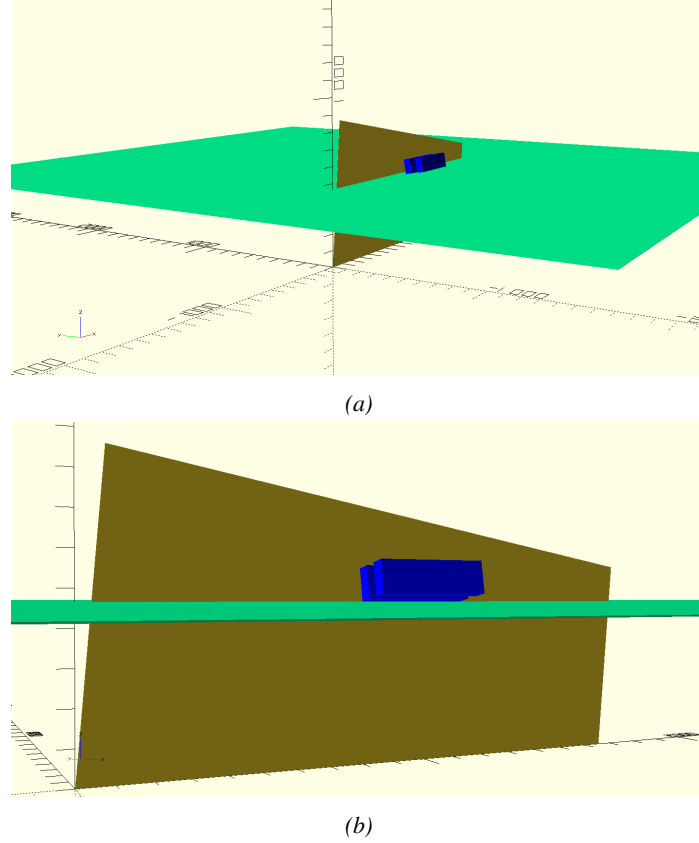


Figure 6.10: Representation of the layout used for the simulations of the test setup. The RPC is represented as a yellow trapezoid while the two scintillators as blue cuboids looking at the sky. A green plane corresponds to the muon generation plane within the simulation. Figure 6.4a shows a global view of the simulated setup. Figure 6.4b shows a zoomed view that allows to see the 2 scintillators as well as the full RPC plane.

scope inclinations. Moreover, the threshold applied on the PMT signals has been included into the simulation in the form of a cut. In the approximation of uniform scintillators, it has been considered that the threshold can be understood as the minimum distance particles need to travel through the scintillating material to give a strong enough signal. Particles that travel a distance smaller than the set "threshold" are thus not detected by the telescope and cannot trigger the data taking. Finally, the FEE threshold also has been considered in a similar way. The mean momentum of horizontal cosmic rays is higher than those of vertical ones but the stopping power of matter for momenta ranging from 1 GeV to 1 TeV stays comparable. It is then possible to assume that the mean number of primary e^-/ion

pairs per unit length will stay similar and thus, depending on the applied discriminator threshold, muons with the shortest path through the gas volume will deposit less charge and induce a smaller signal on the pick-up strips that could eventually not be detected. These two thresholds also restrain the overall geometrical acceptance of the system.

6.2.3.2 Simulation procedure

The simulation software has been designed using C++ and the output data is saved into ROOT histograms. Simulations start for a threshold T_{scint} varying in a range from 0 to 45 mm in steps of 5 mm, where $T_{scint} = 0$ mm corresponds to the case where there isn't any threshold apply on the input signal while $T_{scint} = 45$ mm, which is the scintillator thickness, is the case where muons cannot arrive orthogonally onto the scintillator surface. For a given T_{scint} , a set of RPC thresholds are considered. The RPC threshold, T_{RPC} varies from 2 mm, the thickness of the gas volume, to 3 mm in steps of 0.25 mm. For each $(T_{scint}; T_{RPC})$ pair, $N_\mu = 10^8$ muons are randomly generated inside the muon plane described in the previous paragraph with an azimuthal angle θ chosen to follow a $\cos^2\theta$ distribution.

Planes are associated to each surface of the scintillators. Knowing muon position into the muon plane and its direction allows us, by assuming that muons travel in a straight line, to compute the intersection of the muon track with these planes. Applying conditions to the limits of the surfaces of the scintillator faces then gives us an answer to whether or not the muon passed through the scintillators. In the case the muon has indeed passed through the telescope, the path through each scintillator is computed and muons whose path was shorter than T_{scint} are rejected and are thus considered as having not interacted with the setup.

On the contrary, if the muon is labeled as good, its position within the RPC plane is computed and the corresponding strip, determined by geometrical tests in the case the distance through the gas volume was enough not to be rejected because of T_{RPC} , gets a hit and several histograms are filled in order to keep track of the generation point on the muon plane, the intersection points of the reconstructed muons within the telescope, or on the RPC plane, the path traveled through each individual scintillator or the gas volume, as well as other histograms. Moreover, muons fill different histograms whether they are forward or backward coming muons. They are discriminated according to their direction components. When a muon is generated, an (x, y, z) position is assigned into the muon plane as well as a $(\theta; \phi)$ pair that gives us the direction it's coming from. This way, muons satisfying the condition $0 \leq \phi < \pi$ are designated as backward coming muons while muons satisfying $\pi \leq \phi < 2\pi$ as forward coming muons.

This simulation is then repeated for different telescope inclinations ranging in between 4 and 20° and varying in steps of 2°. Due to this inclination and to the vertical position of the detector under test, the muon distribution reconstructed in

the detector plane is asymmetrical. The choice as been made to chose a skew distribution formula to fit the data built as the multiplication of gaussian and sigmoidal curves together. A typical gaussian formula is given as 6.1 and has three free parameters as A_g , its amplitude, \bar{x} , its mean value and σ , its root mean square. Sigmoidal curves as given by formula 6.2 are functions converging to 0 and A_s as x diverges. The inflexion point is given as x_i and λ is proportional to the slope at $x = x_i$. In the limit where $\lambda \rightarrow \infty$, the sigmoid becomes a step function.

$$g(x) = A_g e^{-\frac{(x-\bar{x})^2}{2\sigma^2}} \quad (6.1)$$

$$s(x) = \frac{A_s}{1 + e^{-\lambda(x-x_i)}} \quad (6.2)$$

Finally, a possible representation of a skew distribution is given by formula 6.3 and is the product of 6.1 and 6.2. Naturally, here $A_{sk} = A_g \times A_s$ and represents the theoretical maximum in the limit where the skew tends to a gaussian function.

$$sk(x) = g(x) \times s(x) = A_{sk} \frac{e^{-\frac{(x-\bar{x})^2}{2\sigma^2}}}{1 + e^{-\lambda(x-x_i)}} \quad (6.3)$$

6.2.3.3 Results

Influence of T_{scint} on the muon distribution

Influence of T_{RPC} on the muon distribution

Influence of the telescope inclination on the muon distribution

Comparison to data taken at GIF without irradiation

6.2.4 Photon flux at GIF

6.2.4.1 Expectations from simulations

In order to understand and evaluate the γ flux in the GIF area, simulations had been conducted in 1999 and published by S. Agosteo et al [4]. Table 6.1 presented in this article gives us the γ flux for different distances D to the source. This simulation was done using GEANT and a Monte Carlo N-Particle (MCNP) transport

Nominal ABS	Photon flux F [$s^{-1}cm^{-2}$]			
	at $D = 50$ cm	at $D = 155$ cm	at $D = 300$ cm	at $D = 400$ cm
1	$0.12 \cdot 10^8 \pm 0.2\%$	$0.14 \cdot 10^7 \pm 0.5\%$	$0.45 \cdot 10^6 \pm 0.5\%$	$0.28 \cdot 10^6 \pm 0.5\%$
2	$0.68 \cdot 10^7 \pm 0.3\%$	$0.80 \cdot 10^6 \pm 0.8\%$	$0.25 \cdot 10^6 \pm 0.8\%$	$0.16 \cdot 10^6 \pm 0.6\%$
5	$0.31 \cdot 10^7 \pm 0.4\%$	$0.36 \cdot 10^6 \pm 1.2\%$	$0.11 \cdot 10^6 \pm 1.2\%$	$0.70 \cdot 10^5 \pm 0.9\%$

Table 6.1: Total photon flux ($E\gamma \leq 662$ keV) with statistical error predicted considering $a^{137}\text{Cs}$ activity of 740 GBq at different values of the distance D to the source along the x -axis of irradiation field [4].

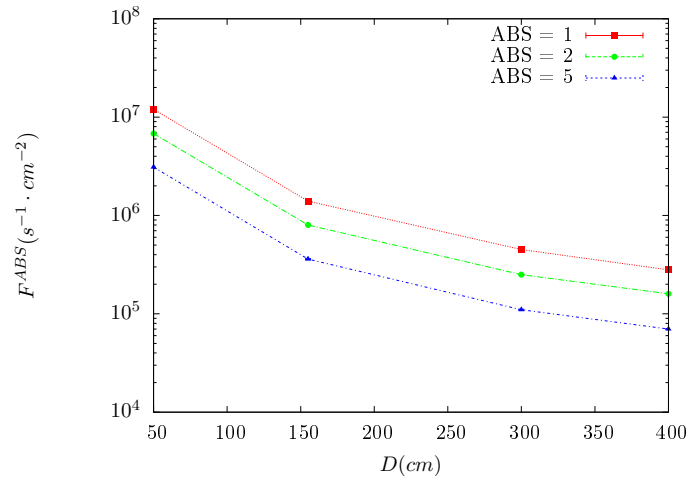


Figure 6.11: γ flux $F(D)$ is plot using values from table 6.1. As expected, the plot shows similar attenuation behaviours with increasing distance for each absorption factors.

code, and the flux F is given in number of γ per unit area and unit time along with the estimated error from these packages expressed in %.

The simulation doesn't directly provides us with an estimated flux at the level of our RPC. First of all, it is needed to extract the value of the flux from the available data contained in the original paper and then to estimate the flux in 2014 at the time the experimentation took place. Figure 6.11 that contains the data from Table 6.1. In the case of a pointlike source emitting isotrope and homogeneous gamma radiations, the gamma flux F at a distance D to the source with respect to a reference point situated at D_0 where a known flux F_0 is measured will be expressed like in Equation 6.4, assuming that the flux decreases as $1/D^2$, where c is a fitting factor.

$$F^{ABS} = F_0^{ABS} \times \left(\frac{cD_0}{D} \right)^2 \quad (6.4)$$

By rewriting Equation 6.4, it comes that :

$$c = \frac{D}{D_0} \sqrt{\frac{F^{ABS}}{F_0^{ABS}}} \quad (6.5)$$

$$\Delta c = \frac{c}{2} \left(\frac{\Delta F^{ABS}}{F^{ABS}} + \frac{\Delta F_0^{ABS}}{F_0^{ABS}} \right) \quad (6.6)$$

Finally, using Equation 6.5 and the data in Table 6.1 with $D_0 = 50$ cm as reference point, we can build Table 6.2. It is interesting to note that c for each value of D doesn't depend on the absorption factor.

Nominal ABS	Correction factor c		
	at $D = 155$ cm	at $D = 300$ cm	at $D = 400$ cm
1	$1.059 \pm 0.70\%$	$1.162 \pm 0.70\%$	$1.222 \pm 0.70\%$
2	$1.063 \pm 1.10\%$	$1.150 \pm 1.10\%$	$1.227 \pm 0.90\%$
5	$1.056 \pm 1.60\%$	$1.130 \pm 1.60\%$	$1.202 \pm 1.30\%$

Table 6.2: Correction factor c is computed thanks to formulae 6.5 taking as reference $D_0 = 50$ cm and the associated flux F_0^{ABS} for each absorption factor available in table 6.1.

For the range of D/D_0 values available, it is possible to use a simple linear fit to get the evolution of c . The linear fit will then use only 2 free parameters, a and b , as written in Equation 6.7. This gives us the results showed in Figure 6.12. Figure 6.12b confirms that using only a linear fit to extract c is enough as the evolution of the rate that can be obtained superimposes well on the simulation points.

$$c \left(\frac{D}{D_0} \right) = a \frac{D}{D_0} + b \quad (6.7)$$

$$F^{ABS} = F_0^{ABS} \left(a + \frac{bD_0}{D} \right)^2 \quad (6.8)$$

$$\Delta F^{ABS} = F^{ABS} \left[\frac{\Delta F_0^{ABS}}{F_0^{ABS}} + 2 \frac{\Delta a + \Delta b \frac{D_0}{D}}{a + \frac{bD_0}{D}} \right] \quad (6.9)$$

In the case of the 2014 GIF tests, the RPC plane is located at a distance $D = 206$ cm to the source. Moreover, to estimate the strength of the flux in 2014, it is necessary to consider the nuclear decay through time associated to the Cesium source whose half-life is well known ($t_{1/2} = (30.05 \pm 0.08)$ y). The very first source activity measurement has been done on the 5th of March 1997 while the

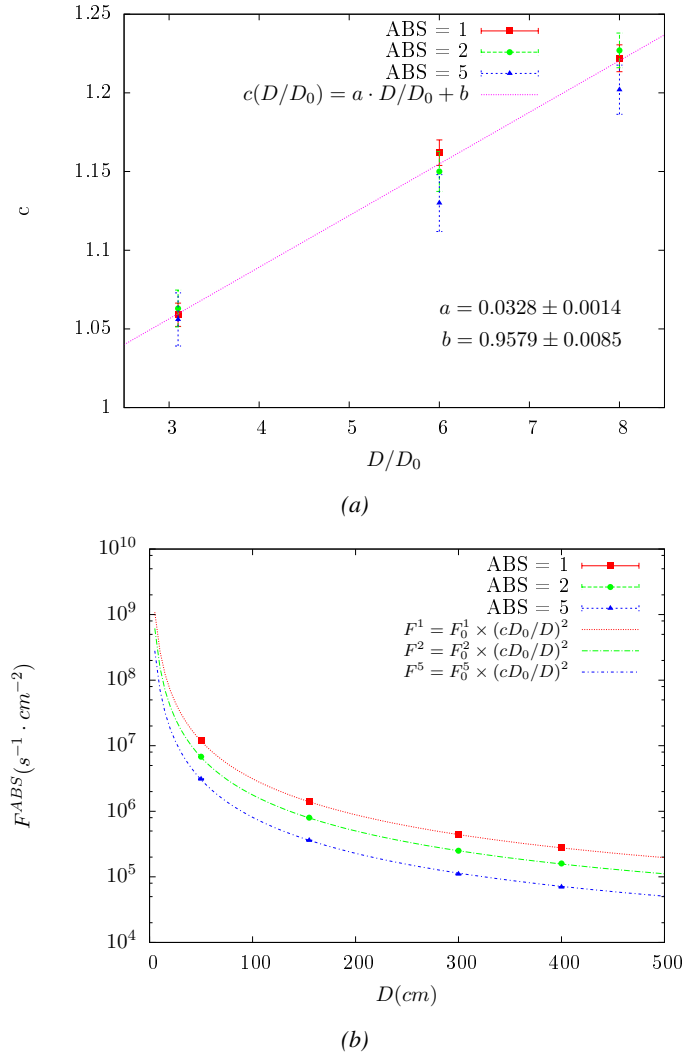


Figure 6.12: Figure 6.12a shows the linear approximation fit done via formulae 6.7 on data from table 6.2. Figure 6.12b shows a comparison of this model with the simulated flux using a and b given in figure 6.12a in formulae 6.4 and the reference value $D_0 = 50cm$ and the associated flux for each absorption factor F_0^{ABS} from table 6.1

633 GIF tests were done in between the 20th and the 31st of August 2014, i.e. at a
 634 time $t = (17.47 \pm 0.02)$ y resulting in an attenuation of the activity from 740 GBq
 635 in 1997 to 494 GBq in 2014. All the needed information to extrapolate the flux
 636 through our detector in 2014 has now been assembled, leading to the Table 6.3. It
 637 is interesting to note that for a common RPC sensitivity to γ of $2 \cdot 10^{-3}$, the order

of magnitude of the estimated hit rate per unit area is of the order of the kHz for the fully opened source. Moreover, taking profit of the two working absorbers, it will be possible to scan background rates at 0 Hz, ~ 300 Hz as well as ~ 600 Hz. Without source, a good estimate of the intrinsic performance will be available. Then at 300 Hz, the goal will be to show that the detectors fulfill the performance certification of CMS RPCs. Then a first idea of the performance of the detectors at higher background will be provided with absorption factors 2 (~ 600 Hz) and 1 (no absorption). *[Here I will also put a reference to the plot showing the estimated background rate at the level of RE3/1 in the case of HL-LHC but this one being in another chapter, I will do it later.]*

Nominal ABS	Photon flux F [$\text{s}^{-1}\text{cm}^{-2}$]			Hit rate/unit area [Hz cm^{-2}] at $D^{2014} = 206$ cm
	at $D_0^{1997} = 50$ cm	at $D^{1997} = 206$ cm	at $D^{2014} = 206$ cm	
1	$0.12 \cdot 10^8 \pm 0.2\%$	$0.84 \cdot 10^6 \pm 0.3\%$	$0.56 \cdot 10^6 \pm 0.3\%$	1129 ± 32
2	$0.68 \cdot 10^7 \pm 0.3\%$	$0.48 \cdot 10^6 \pm 0.3\%$	$0.32 \cdot 10^6 \pm 0.3\%$	640 ± 19
5	$0.31 \cdot 10^7 \pm 0.4\%$	$0.22 \cdot 10^6 \pm 0.3\%$	$0.15 \cdot 10^6 \pm 0.3\%$	292 ± 9

Table 6.3: The data at D_0 in 1997 is taken from [4]. In a second step, using Equations 6.8 and 6.9, the flux at D can be estimated in 1997. Then, taking into account the attenuation of the source activity, the flux at D can be estimated at the time of the tests in GIF in 2014. Finally, assuming a sensitivity of the RPC to γ $s = 2 \cdot 10^{-3}$, an estimation of the hit rate per unit area is obtained.

6.2.4.2 Dose measurements

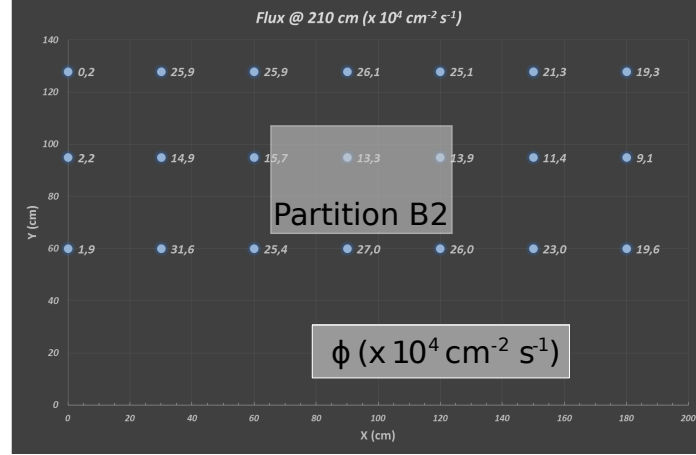


Figure 6.13: Dose measurements has been done in a plane corresponding to the tents front side. This plan is 1900 mm away from the source. As explained in the first chapter, a lens-shaped lead filter provides a uniform photon flux in the vertical plan orthogonal to the beam direction. If the second line of measured fluxes is not taken into account because of lower values due to experimental equipments in the way between the source and the tent, the uniformity of the flux is well showed by the results.

6.3 Longevity tests at GIF++

This study implies a monitoring of the performance of the detectors probed using a high intensity muon beam in a irradiated environment by periodically measuring their rate capability, the dark current running through them and the bulk resistivity of the Bakelite composing their electrodes. GIF++, with its very intense ^{137}Cs source, provides the perfect environment to perform such kind of tests. Assuming a maximum acceleration factor of 3, it is expected to accumulate the equivalent charge in 1.7 years.

As the maximum background is found in the endcap, the choice naturally was made to focus the GIF++ longevity studies on endcap chambers. Most of the RPC system was installed in 2007. Nevertheless, the large chambers in the fourth endcap (RE4/2 and RE4/3) have been installed during LS1 in 2014. The Bakelite of these two different productions having different properties, four spare chambers of the present system were selected, two RE2,3/2 spares and two RE4/2 spares. Having two chambers of each type allows to always keep one of them non irradiated as reference, the performance evolution of the irradiated chamber being then compared through time to the performance of the non irradiated one.

The performance of the detectors under different level of irradiation is measured periodically during dedicated test beam periods using the H4 muon beam. In be-

tween these test beam periods, the two RE2,3/2 and RE4/2 chambers selected for this study are irradiated by the ^{137}Cs source in order to accumulate charge and the gamma background is monitored, as well as the currents. The two remaining chambers are kept non-irradiated as reference detectors. Due to the limited gas flow in GIF++, the RE4 chamber remained non-irradiated until end of November 2016 where a new mass flow controller has been installed allowing for bigger volumes of gas to flow in the system.

Figures 6.14 and 6.15 give us for different test beam periods, and thus for increasing integrated charge through time, a comparison of the maximum efficiency, obtained using a sigmoid-like function, and of the working point of both irradiated and non irradiated chambers [7]. No aging is yet to see from this data, the shifts in γ rate per unit area in between irradiated and non irradiated detectors and RE2 and RE4 types being easily explained by a difference of sensitivity due to the various Bakelite resistivities of the HPL electrodes used for the electrode production.

Collecting performance data at each test beam period allows us to extrapolate the maximum efficiency for a background hit rate of 300 Hz/cm^2 corresponding to the expected HL-LHC conditions. Aging effects could emerge from a loss of efficiency with increasing integrated charge over time, thus Figure 6.16 helps us understand such degradation of the performance of irradiated detectors in comparison with non irradiated ones. The final answer for an eventual loss of efficiency is given in Figure 6.17 by comparing for both irradiated and non irradiated detectors the efficiency sigmoids before and after the longevity study. Moreover, to complete the performance information, the Bakelite resistivity is regularly measured thanks to A_g scans (Figure 6.18) and the noise rate is monitored weekly during irradiation periods (Figure 6.19). At the end of 2016, no signs of aging were observed and further investigation is needed to get closer to the final integrated charge requirements proposed for the longevity study of the present CMS RPC sub-system.

6.3.1 Description of the Data Acquisition

For the longevity studies, four spare chambers of the present system are used. Two spare RPCs of the RE2,3 stations as well as two spare RPCs from the new RE4 stations have been mounted in a Trolley. Six RE4 gaps are also placed in the trolley. The trolley is placed inside the GIF++ in the upstream region of the bunker, taking the cesium source as a reference. The trolley is oriented for the detection surface of the chambers to be orthogonal to the beam line. The system can be moved along the orthogonal plane in order to have the beam in all η -partitions. For the aging the trolley is moved outside the beam line and is placed in a distance of 5.2 m to the source, which irradiates the bunker using an attenuation filter of 2.2 which corresponds to a fluence of 10^7 gamma/cm^2 . **(numbers from simulation needed)**

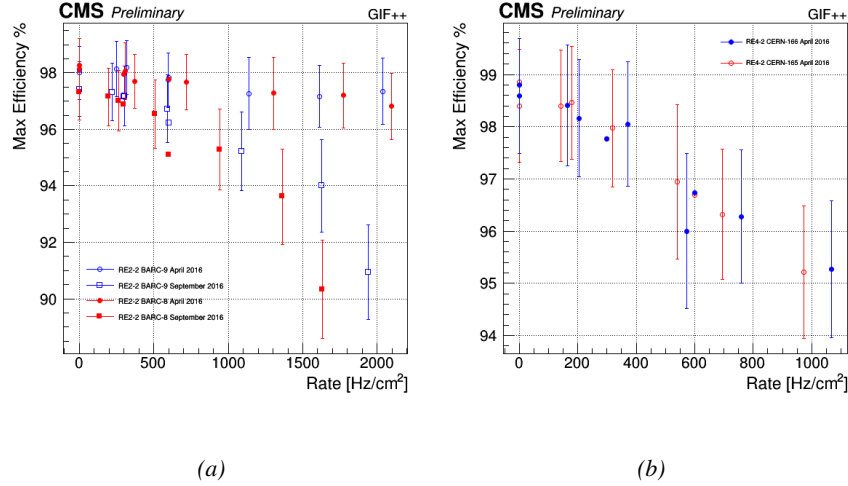


Figure 6.14: Evolution of the maximum efficiency for RE2 (6.14a) and RE4 (6.14b) chambers with increasing extrapolated γ rate per unit area at working point. Both irradiated (blue) and non irradiated (red) chambers are shown.

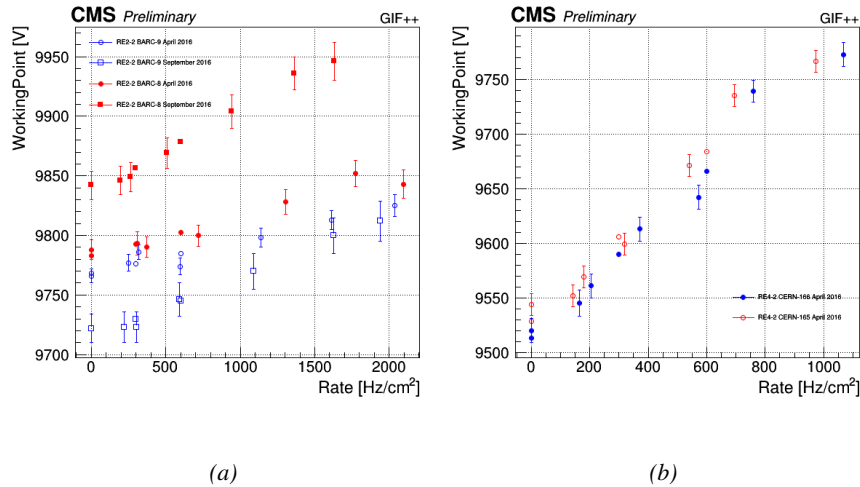


Figure 6.15: Evolution of the working point for RE2 (6.15a) and RE4 (6.15b) with increasing extrapolated γ rate per unit area at working point. Both irradiated (blue) and non irradiated (red) chambers are shown.

707 → Cecilia? Dorothea?)(Alexis : Here do you want to talk about fluence, or
 708 current? I though fluence was to talk about a spherical particle emission
 709 whereas in our case at GIF, there is a lead lens to reshape the gamma emission)

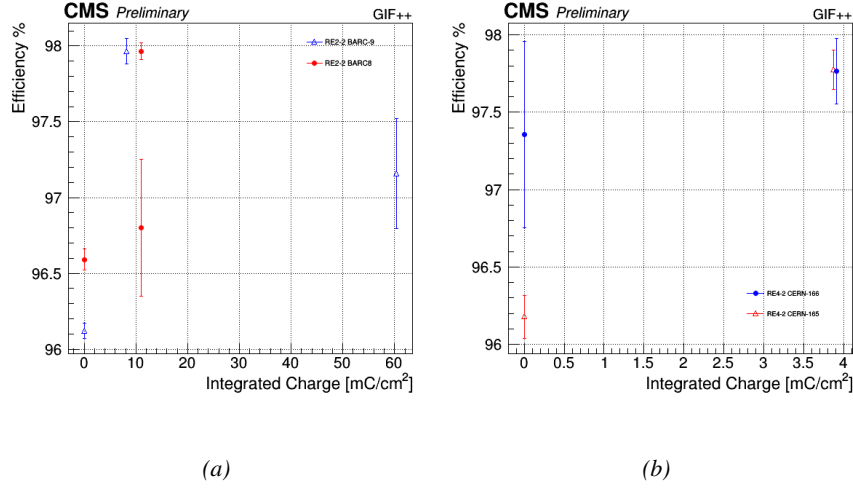


Figure 6.16: Evolution of the maximum efficiency at HL-LHC conditions, i.e. a background hit rate per unit area of 300 Hz/cm², with increasing integrated charge for RE2 (6.16a) and RE4 (6.16b) detectors. Both irradiated (blue) and non irradiated (red) chambers are shown. The integrated charge for non irradiated detectors is recorded during test beam periods and stays small with respect to the charge accumulated in irradiated chambers.

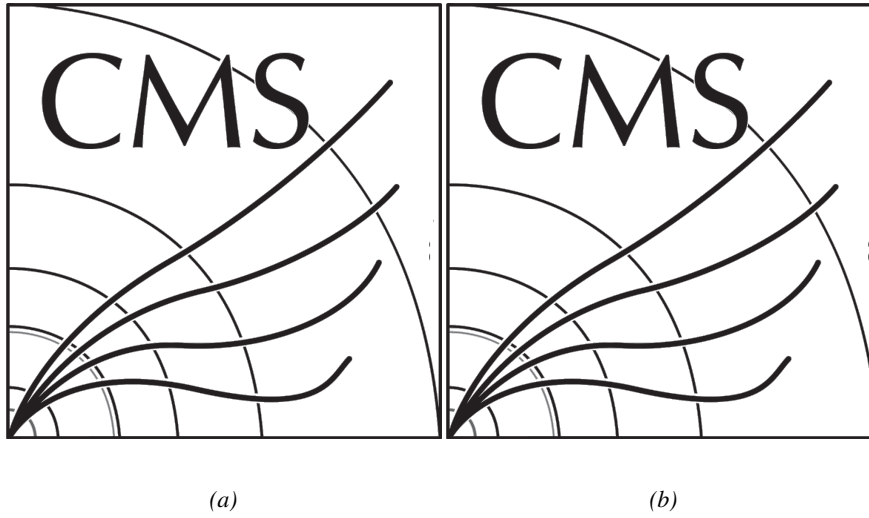


Figure 6.17: Comparison of the efficiency sigmoid before (triangles) and after (circles) irradiation for RE2 (6.17a) and RE4 (6.17b) detectors. Both irradiated (blue) and non irradiated (red) chambers are shown.

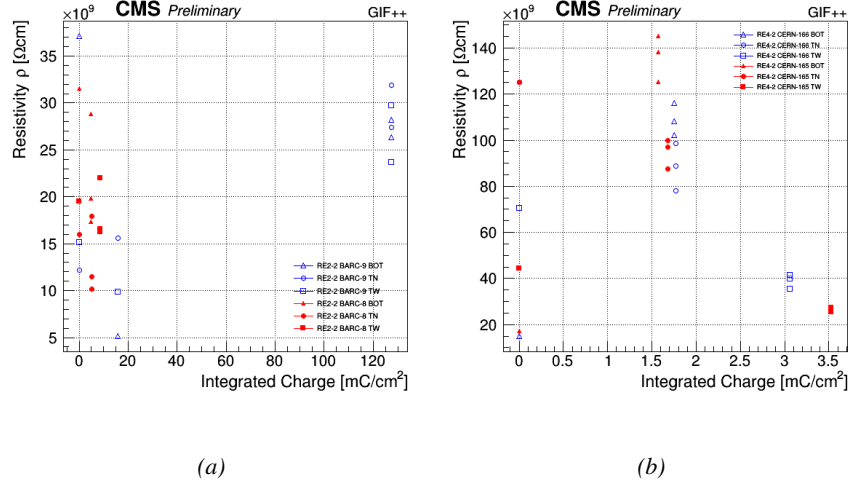


Figure 6.18: Evolution of the Bakelite resistivity for RE2 (6.18a) and RE4 (6.18b) detectors. Both irradiated (blue) and non irradiated (red) chambers are shown.

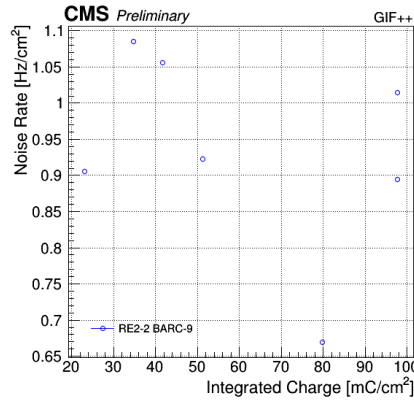


Figure 6.19: Evolution of the noise rate per unit area for the irradiated chamber RE2-2-BARC-9 only.

During GIF++ operation, the data collected can be divided into different categories as several parameters are monitored in addition to the usual RPC performance data. On one hand, to know the performance of a chamber, it is need to measure its efficiency and to know the background conditions in which it is operated. To do this, the hit signals from the chamber are recorded and stored in a ROOT file via a Data Acquisition (DAQ) software. On the other hand, it is also very important to monitor parameters such as environmental pressure and temper-

717 ature, gas temperature and humidity, RPC HV, LV, and currents, or even source
718 and beam status. This is done through the GIF++ web Detector Control Soft-
719 ware (DCS) that stores this information in a database.

720 6.3.1.1 GIF++ RPC DAQ

721 Two different types of tests are conducted on RPCs via the DAQ. Indeed, the per-
722 formance of the detectors is measured periodically during dedicated test beam pe-
723 riods using the H4 muon beam. In between these test beam periods, when the beam
724 is not available, the chambers are irradiated by the ^{137}Cs in order to accumulate
725 deposited charge and the gamma background is measured.

726 RPCs under test are connected through LVDS cables to V1190A Time-to-
727 Digital Converter (TDC) modules manufactured by CAEN. These modules, lo-
728 cated in the rack area outside of the bunker, get the logic signals sent by the cham-
729 bers and save them into their buffers. Due to the limited size of the buffers, the
730 collected data is regularly erased and replaced. A trigger signal is needed for the
731 TDC modules to send the useful data to the DAQ computer via a V1718 CAEN
732 USB communication module.

733 In the case of performance test, the trigger signal used for data acquisition is
734 generated by the coincidence of three scintillators. A first one is placed upstream
735 outside of the bunker, a second one is placed downstream outside of the bunker,
736 while a third one is placed in front of the trolley, close by the chambers. Every time
737 a trigger is sent to the TDCs, i.e. every time a muon is detected, knowing the time
738 delay in between the trigger and the RPC signals, signals located in the right time
739 window are extracted from the buffers and saved for later analysis. Signals are
740 taken in a time window of 400 ns centered on the muon peak (here we could show
741 a time spectrum). On the other hand, in the case of background rate measurement,
742 the trigger signal needs to be "random" not to measure muons but to look at gamma
743 background. A trigger pulse is continuously generated at a rate of 300 Hz using a
744 dual timer. To integrate an as great as possible time, all signals contained within
745 a time window of 10us prior to the random trigger signal are extracted from the
746 buffers and saved for further analysis (here another time spectrum to illustrate
747 could be useful, maybe even place both spectrum together as a single Figure).

748 The signals sent to the TDCs correspond to hit collections in the RPCs. When a
749 particle hits a RPC, it induce a signal in the pickup strips of the RPC readout. If this
750 signal is higher than the detection threshold, a LVDS signal is sent to the TDCs.
751 The data is then organised into 4 branches keeping track of the event number, the
752 hit multiplicity for the whole setup, and the time and channel profile of the hits in
753 the TDCs.

6.3.1.2 RPC current, environmental and operation parameter monitoring

In order to take into account the variation of pressure and temperature between different data taking periods the applied voltage is corrected following the relationship :

$$HV_{eff} = HV_{app} \times \left(0.2 + 0.8 \cdot \frac{P_0}{P} \times \frac{T}{T_0} \right) \quad (6.10)$$

where T_0 (=293 K) and P_0 (=990 mbar) are the reference values.

6.3.2 Tools & Measurements

Insert a short description of the online tools (DAQ, DCS, DQM).

Insert a short description of the offline tools : tracking and efficiency algorithm.

Identify long term aging effects we are monitoring the rates per strip.

6.4 Results and discussions

6.4.1 Preliminary studies results

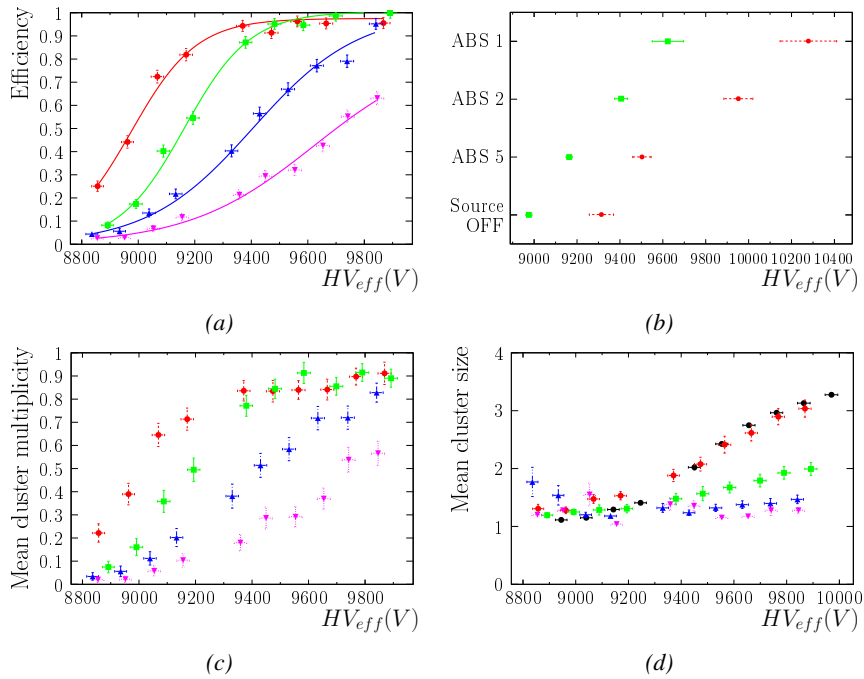


Figure 6.20

765 **6.4.2 Longevity studies results**

7

Simulating a RPC

766

767

768 **7.1 Garfield++ simulation**

769 **7.2 Hybrid simulation**

770 **7.3 Results and discussions**

8

Conclusions and outlooks

771

772

773 **8.1 Conclusions**

774 **8.2 Outlooks**

References

- 776 [1] CERN. Geneva. LHC Experiments Committee. *The CMS muon project :
777 Technical Design Report*. Tech. rep. CERN-LHCC-97-032. CMS Collabora-
778 tion, 1997.
- 779 [2] CERN. Geneva. LHC Experiments Committee. *Technical Proposal for the
780 Phase-II Upgrade of the CMS Detector*. Tech. rep. CERN-LHCC-2015-010.
781 CMS Collaboration, 2015.
- 782 [3] CERN. Geneva. LHC Experiments Committee. *CMS, the Compact Muon
783 Solenoid : technical proposal*. Tech. rep. CERN-LHCC-94-38. CMS Collab-
784 oration, 1994.
- 785 [4] S. Agosteo et al. “A facility for the test of large-area muon chambers at high
786 rates”. In: *NIMA* 452 (2000), pp. 94–104.
- 787 [5] M. Abbrescia et al. “Study of long-term performance of CMS RPC under
788 irradiation at the CERN GIF”. In: *NIMA* 533 (2004), pp. 102–106.
- 789 [6] H.C. Kim et al. “Quantitative aging study with intense irradiation tests for
790 the CMS forward RPCs”. In: *NIMA* 602 (2009), pp. 771–774.
- 791 [7] M. Abbrescia et al. “Cosmic ray tests of double-gap resistive plate chambers
792 for the CMS experiment”. In: *NIMA* 550 (2005), pp. 116–126.



793

794

795

A data acquisition software for VME CAEN TDCs

796

A.1 Introduction

797

Start text here...

B

798

799

Details on the online analysis package

800

B.1 Introduction

801

insert text here



802

803

804

Structure of the hybrid simulation software

805

C.1 Introduction

806

insert text here...

